Electronic supplementary materials *Mendeleev Commun.*, 2026, **36**, 79–81

Novel naphthalene benzimidazole-based materials for potassium metal batteries: revealing the importance of molecular weight for material performance

Yuriy I. Baluda, Alexander V. Mumyatov, Tatyana A. Savinykh, Evgeniya P. Antoshkina, Sergey G. Vasil’ev, Alexander F. Shestakov, Pavel A. Troshin and Olga A. Kraevaya

Table of contents

Figure S1. FTIR spectra of NBI1-NBI3 and NDA. S2

Figure S2. ^{1}H MAS NMR spectra of NBI1. S3

Figure S3. ^{13}C MAS NMR spectra of NBI1. S3

Figure S4. ^{1}H MAS NMR spectra of NBI2. S4

Figure S5. ^{13}C MAS NMR spectra of NBI2. S4

Figure S6. ^{1}H MAS NMR spectra of NBI3. S5

Figure S7. ^{13}C MAS NMR spectra of NBI3. S5

Figure S8. MALDI mass spectra of NBI1 (positive ion mode). S6

Figure S9. MALDI mass spectra of NBI2 (negative ion mode). S6

Figure S10. MALDI mass spectra of NBI3 (negative ion mode). S7

Figure S11. Rate capability of the Li//NBI1 coin cell (a), cycling performance of the Li//NBI1 pouch cell at current density of 100 mA g^{-1} (b), cycling performance (c) and charge-discharge profiles (d) at 100 mA g^{-1} of Li//NBI1 coin cell: 75 cycles in CCCV mode, thereafter in CC mode. S7

Figure S12. Cyclic voltammogram (a), cycling performance at current density of 100 mA g^{-1} (b), rate capability (c) and charge-discharge curves at 100 mA g^{-1} (d) of Li//NBI2 cells. S8

Figure S13. Cyclic voltammogram (a) and cycling performance at current density of 100 mA g^{-1} (b) of Li//NBI3 cells. S8

Figure S14. Cyclic voltammogram (a) and cycling performance at current density of 100 mA g^{-1} (b) of K//NBI1 cells. S9

Figure S15. Cyclic voltammogram (a) and cycling performance at current density of 100 mA g^{-1} (b) of K//NBI3 cells. S9

Figure S16. Trans- (a) and cis-form (b) of NBI fragment. S12

Figure S17. Band gap width as a function of the monomer number for NBIs calculated at the B3LYP/6-31G** level, defined as Eg = E^{HOMO} – E^{LUMO}, and molecular orbitals of NBI2. S13

Figure S18. Two layers of NBI2 (a), distance between the layers after the first step of metalation (b) and the second step of metalation (c), Å. S14

Figure S19. Metalated structures of two layers of NBI2 with different relative shifts between the layers (top view, side view). Interatomic distances are given in the Å. S14

Table S1. Electrochemical performance of NBI2 in potassium cells as compared to previously reported polyimide materials. S15

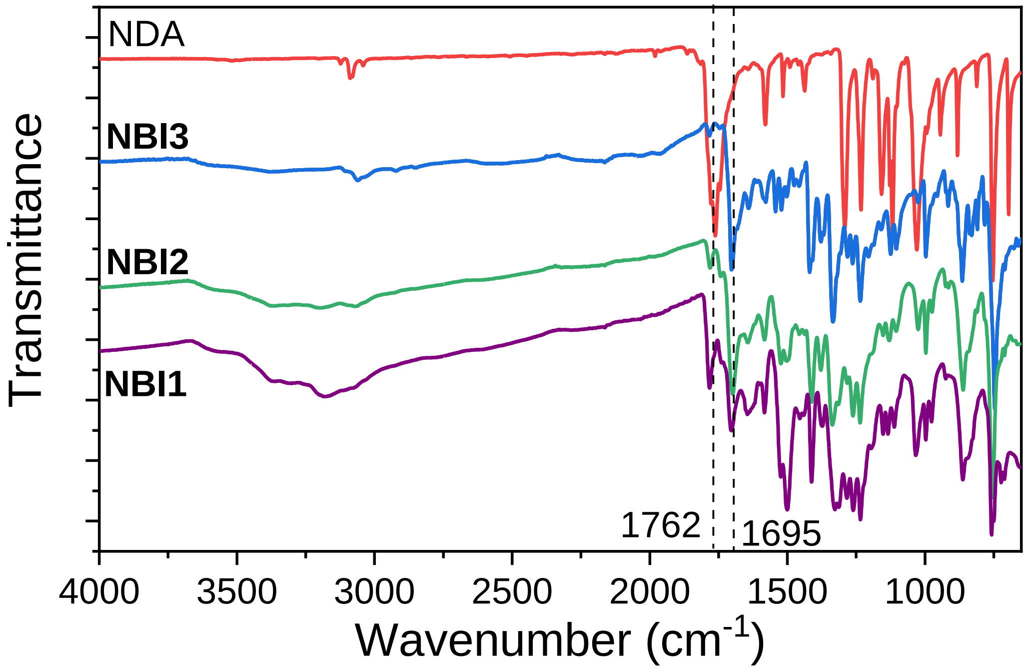

Figure S1. FTIR spectra of **NBI1-NBI3** and **NDA**.

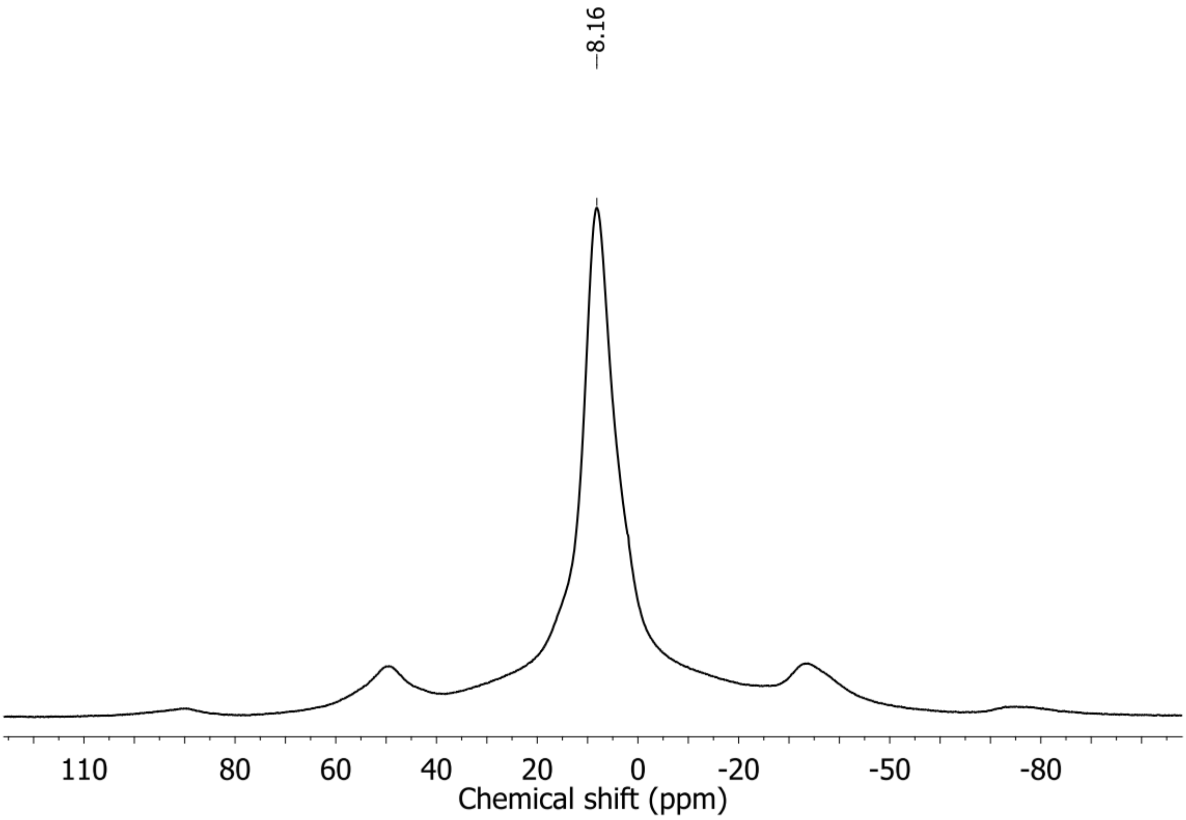

Figure S2. ^{1}H MAS NMR spectra of **NBI1**.

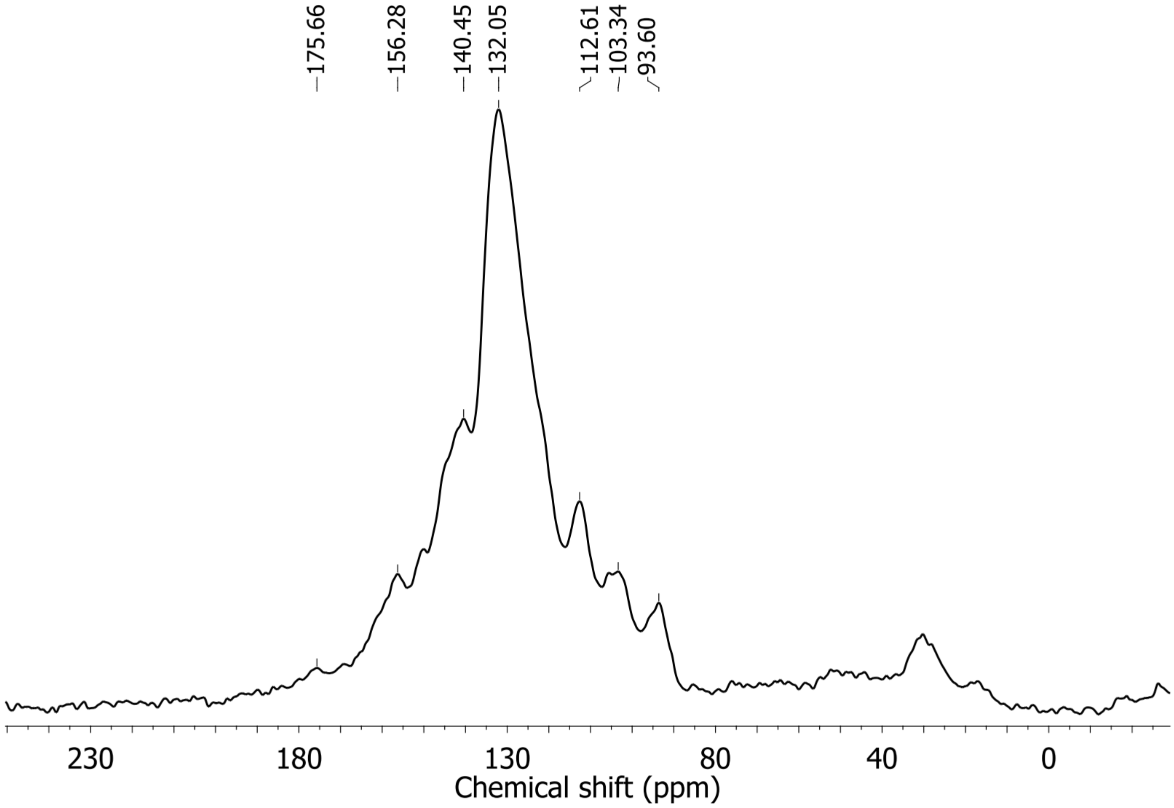

Figure S3. ^{13}C MAS NMR spectra of **NBI1**.

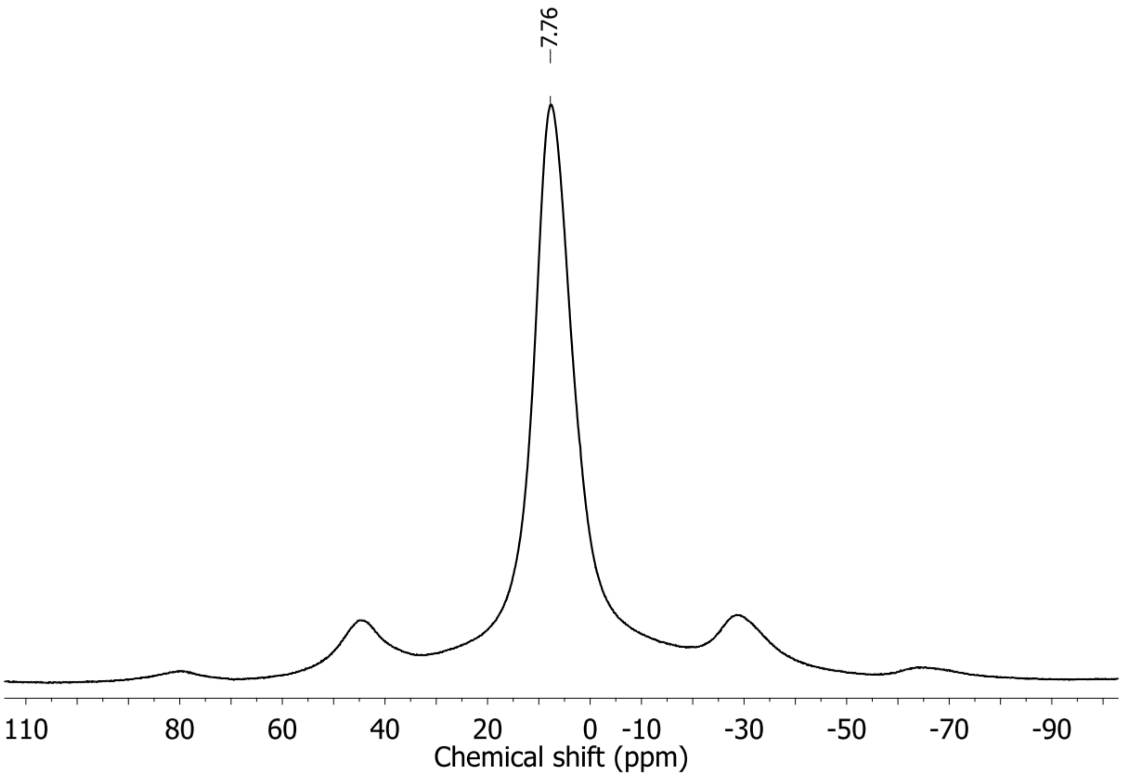

Figure S4. ^{1}H MAS NMR spectra of **NBI2**.

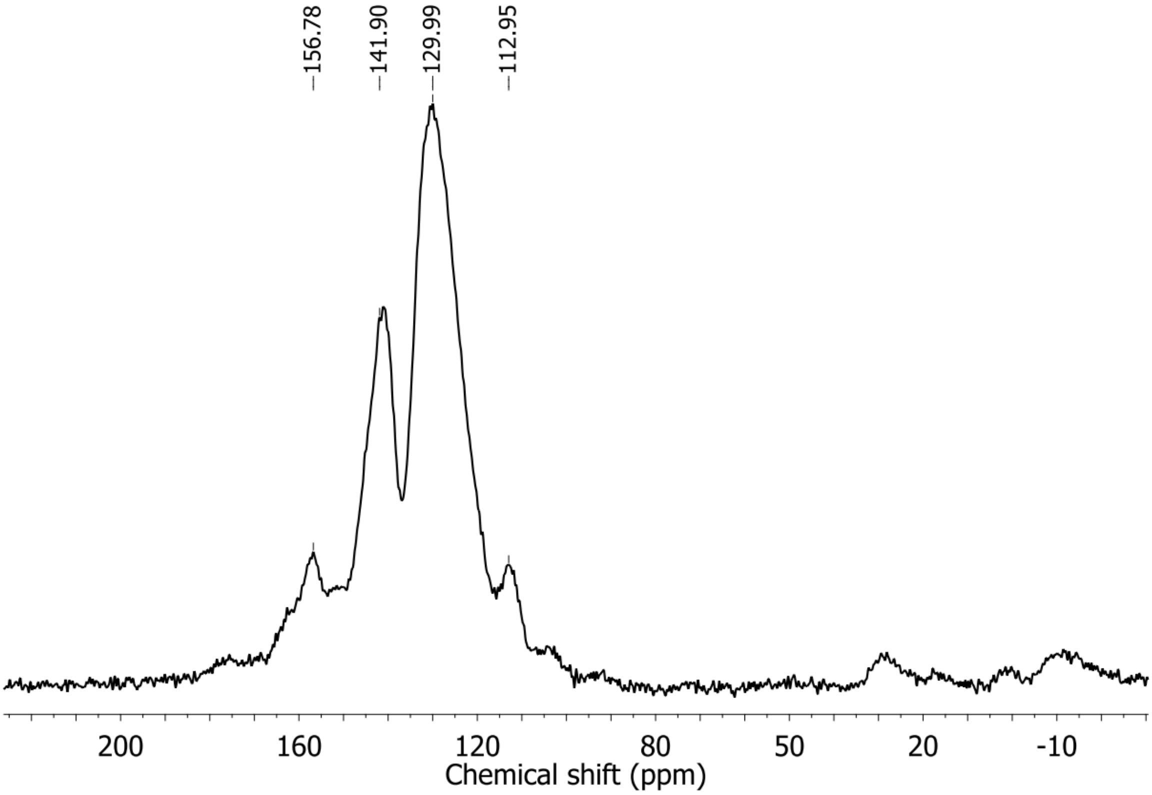

Figure S5. ^{13}C MAS NMR spectra of **NBI2**.

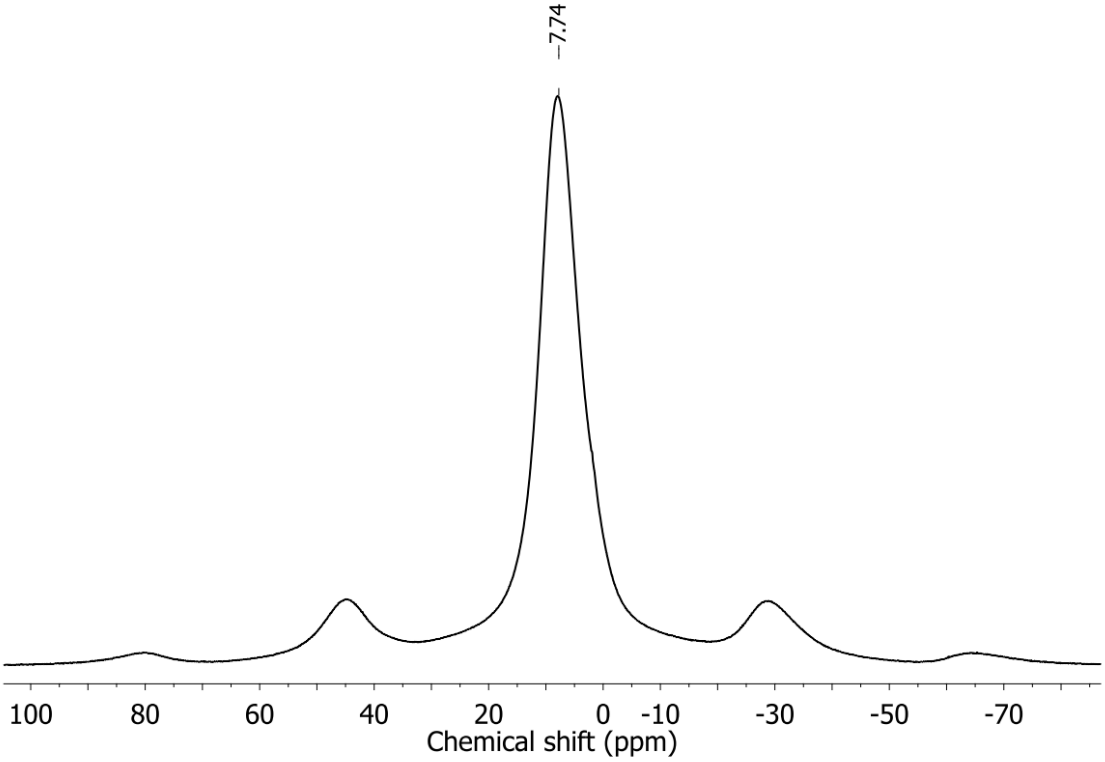

Figure S6. ^{1}H MAS NMR spectra of **NBI3**.

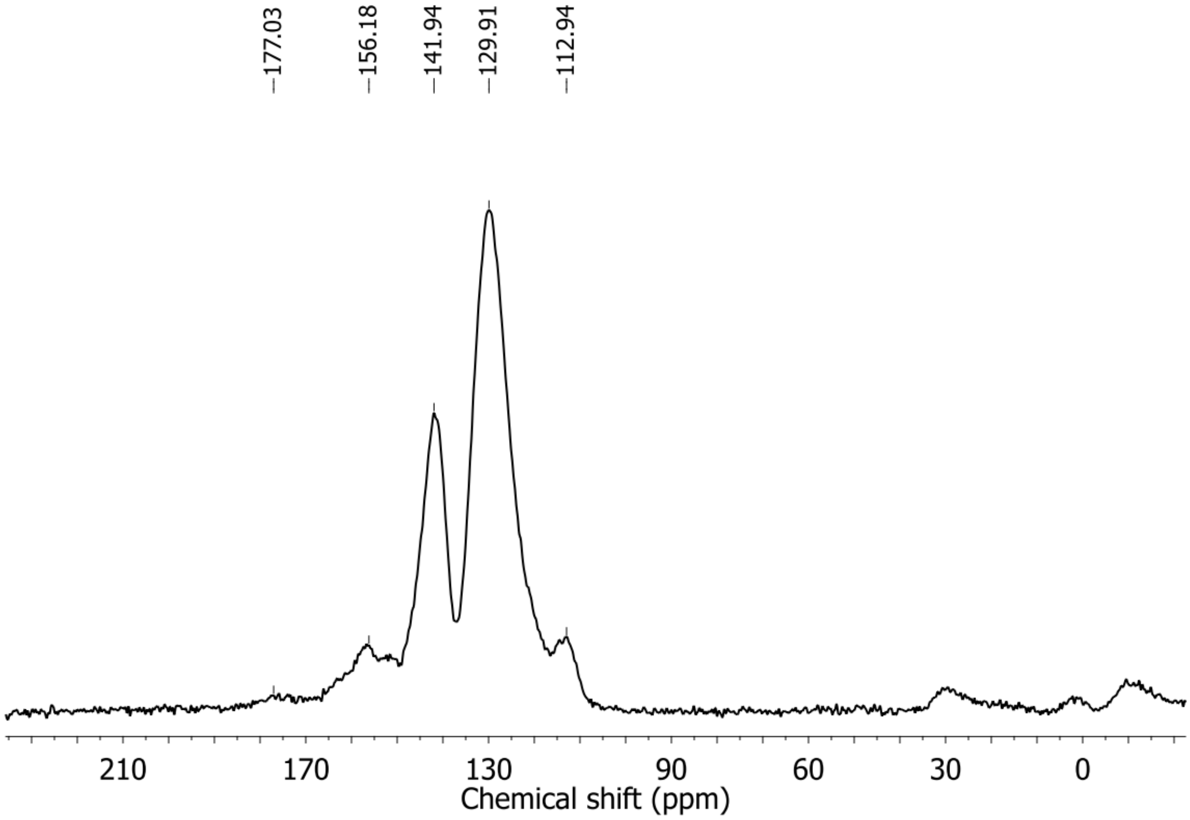

Figure S7. ^{13}C MAS NMR spectra of **NBI3**.

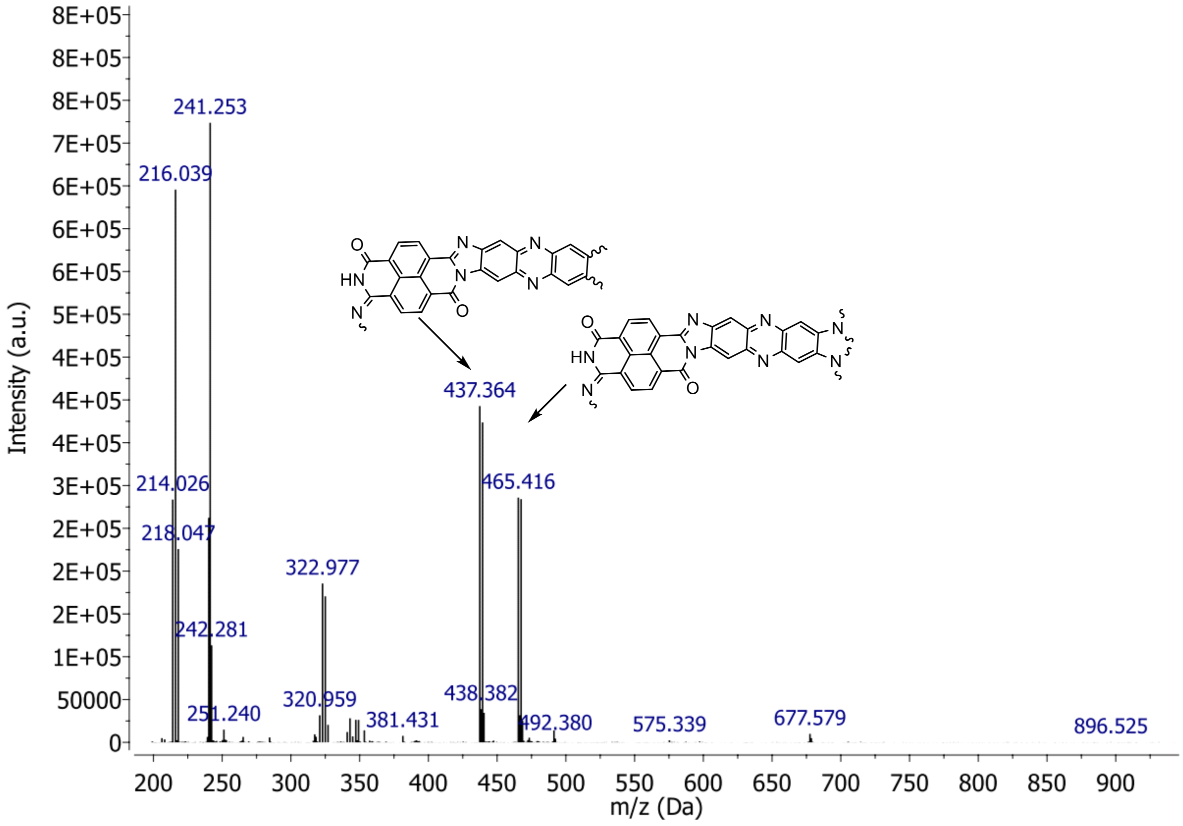

Figure S8. MALDI mass spectra of **NBI1** (positive ion mode).

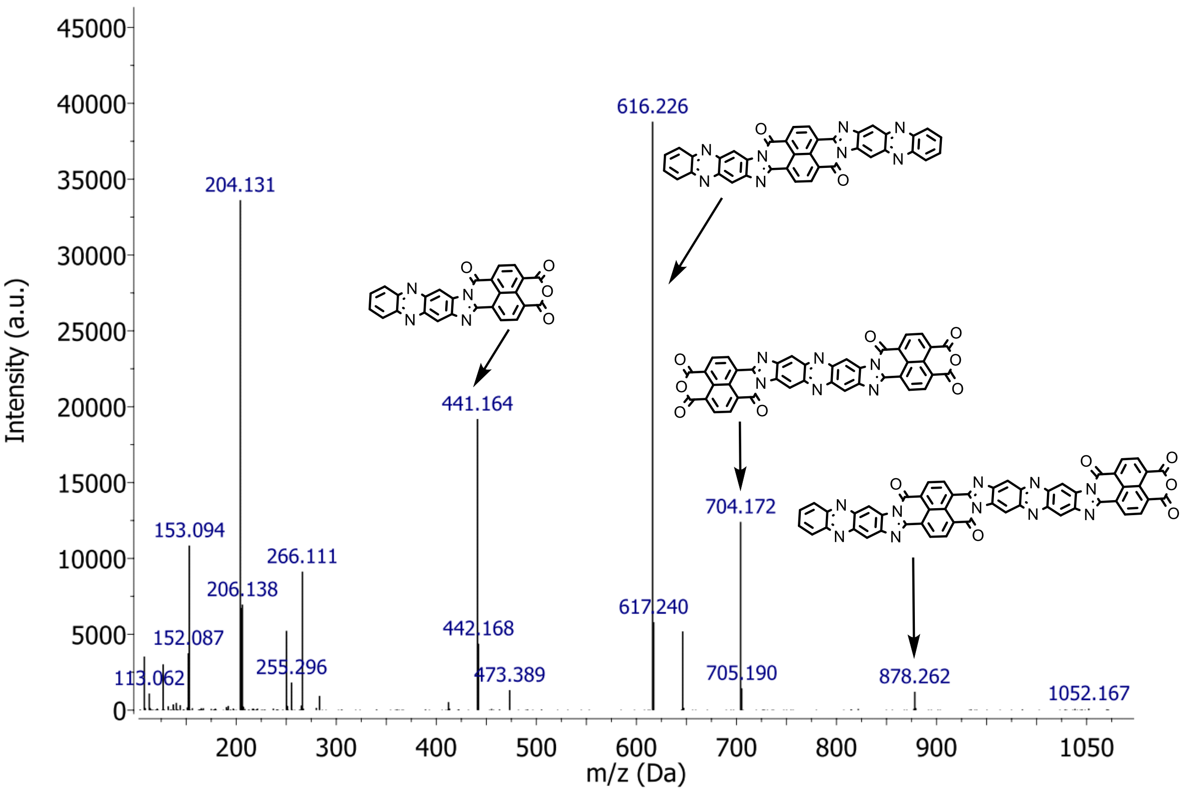

Figure S9. MALDI mass spectra of **NBI2** (negative ion mode).

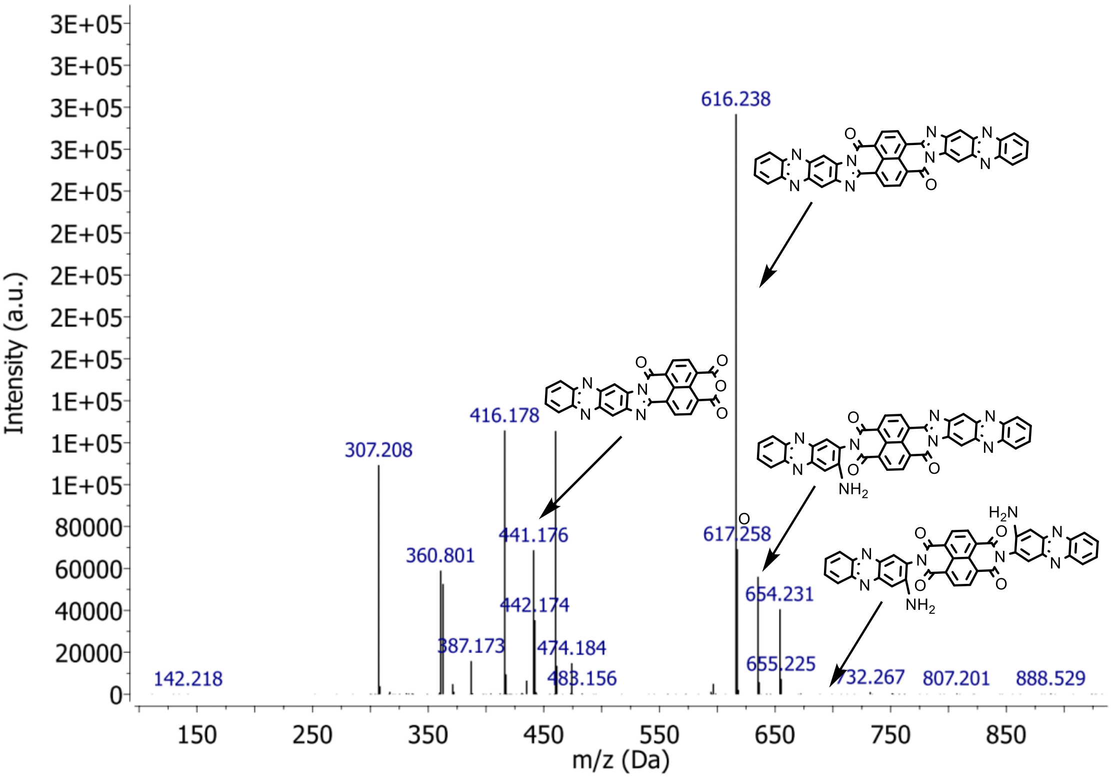

Figure S10. MALDI mass spectra of **NBI3** (negative ion mode).

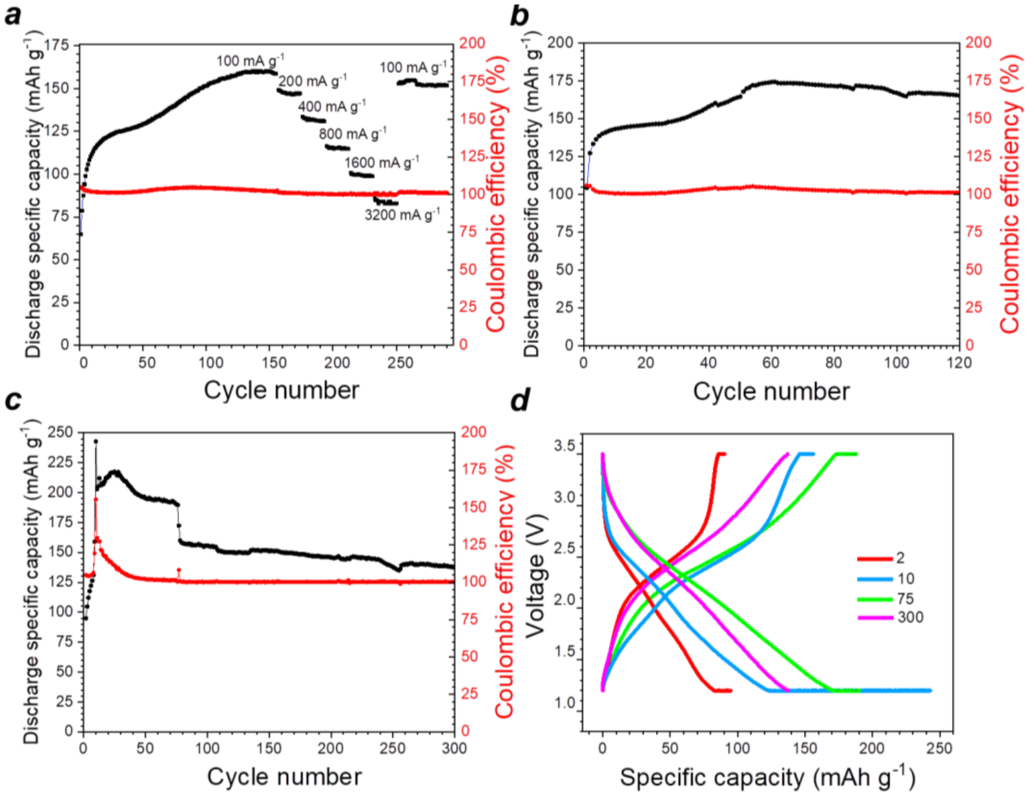

Figure S11. Rate capability of the Li//**NBI1** coin cell (a), cycling performance of the Li//**NBI1** pouch cell at current density of 100 mA g^{-1} (b), cycling performance (c) and charge-discharge profiles (d) at 100 mA g^{-1} of Li//**NBI1** coin cell: 75 cycles in CCCV mode, thereafter in CC mode.

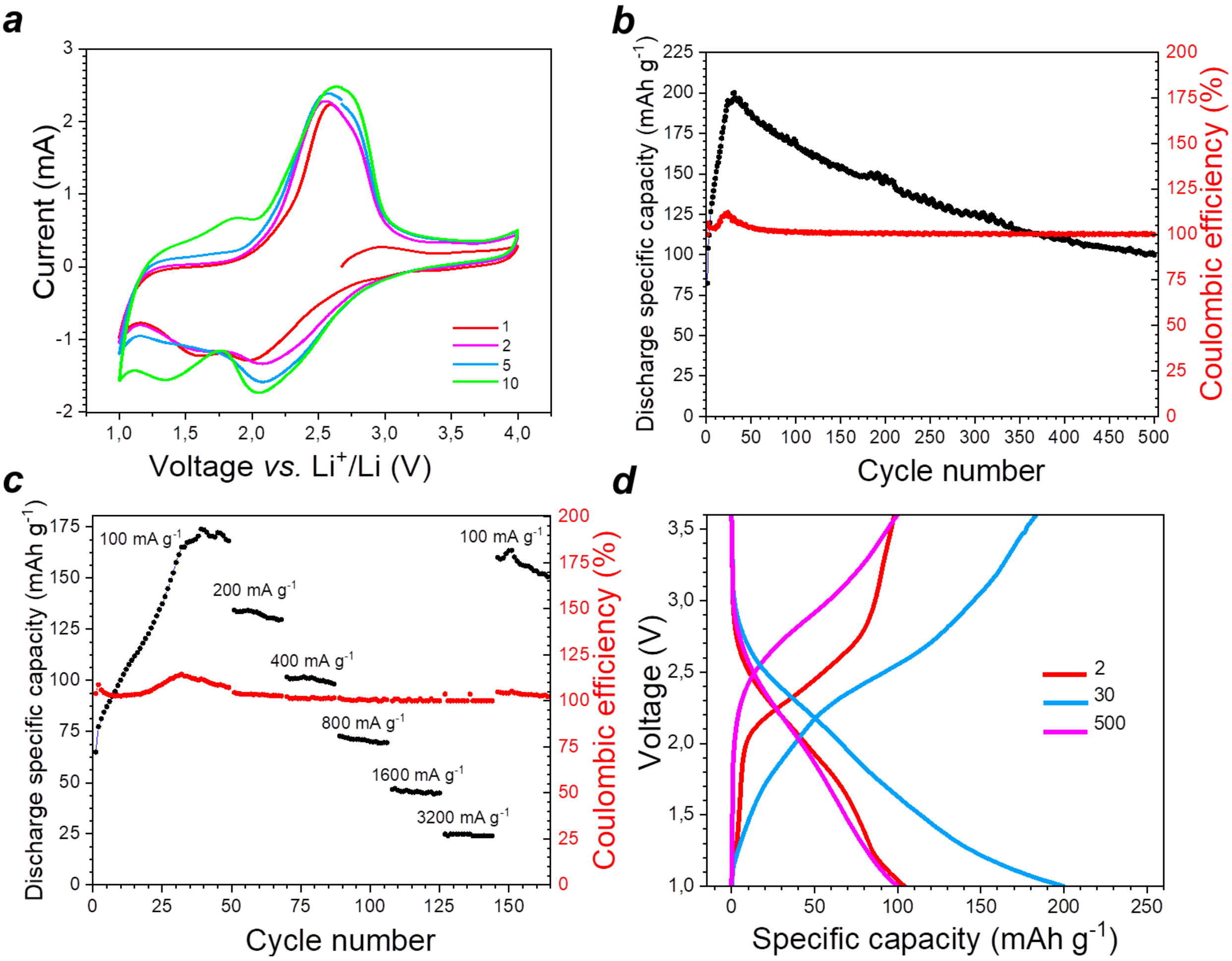

Figure S12. Cyclic voltammogram (a), cycling performance at current density of 100 mA g^{-1} (b), rate capability (c) and charge-discharge curves at 100 mA g^{-1} (d) of Li//**NBI2** cells.

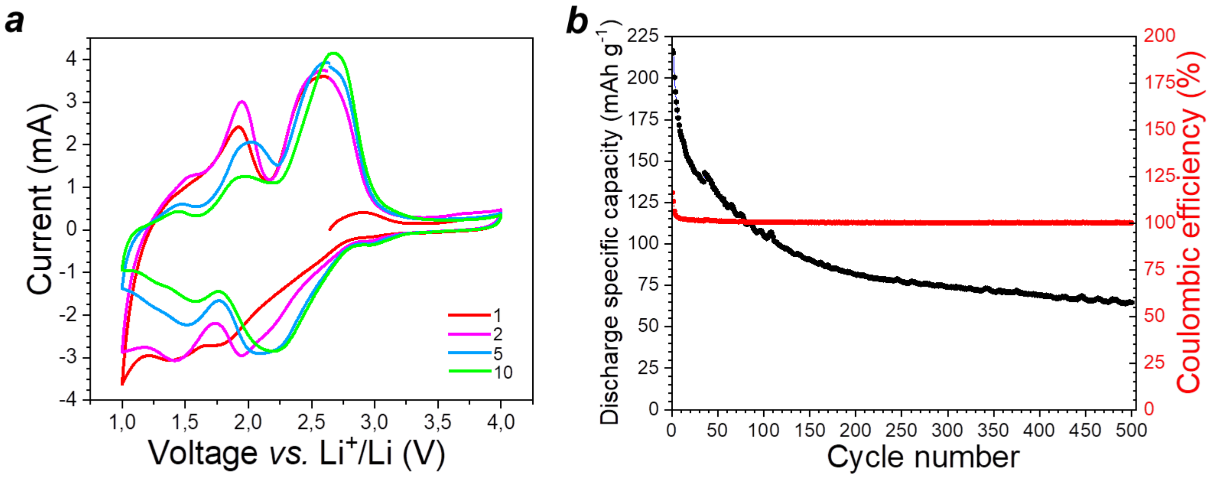

Figure S13. Cyclic voltammogram (a) and cycling performance at current density of 100 mA g^{-1} (b) of Li//**NBI3** cells.

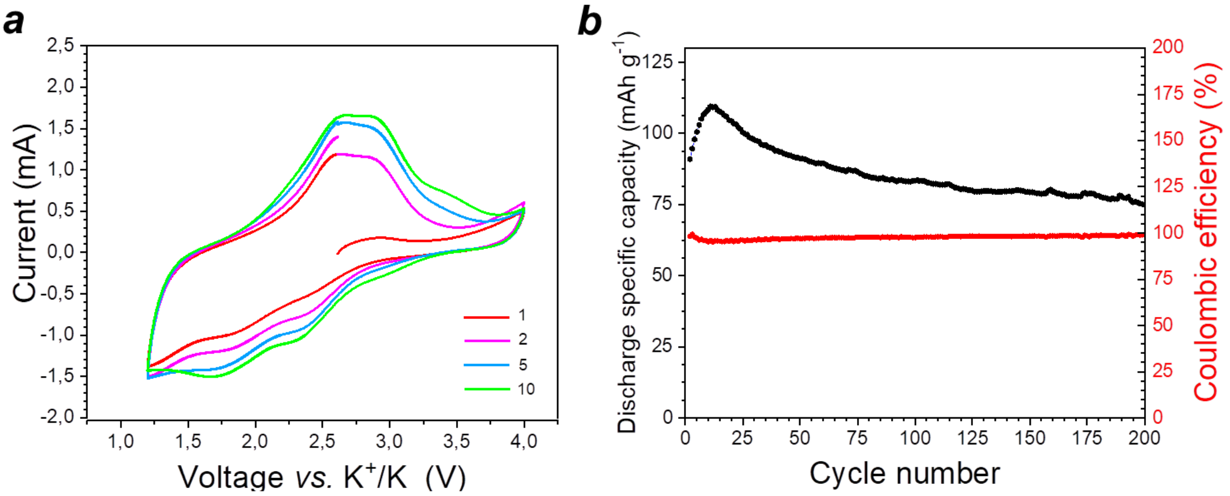

Figure S14. Cyclic voltammogram (a) and cycling performance at current density of 100 mA g^{-1} (b) of K//**NBI1** cells.

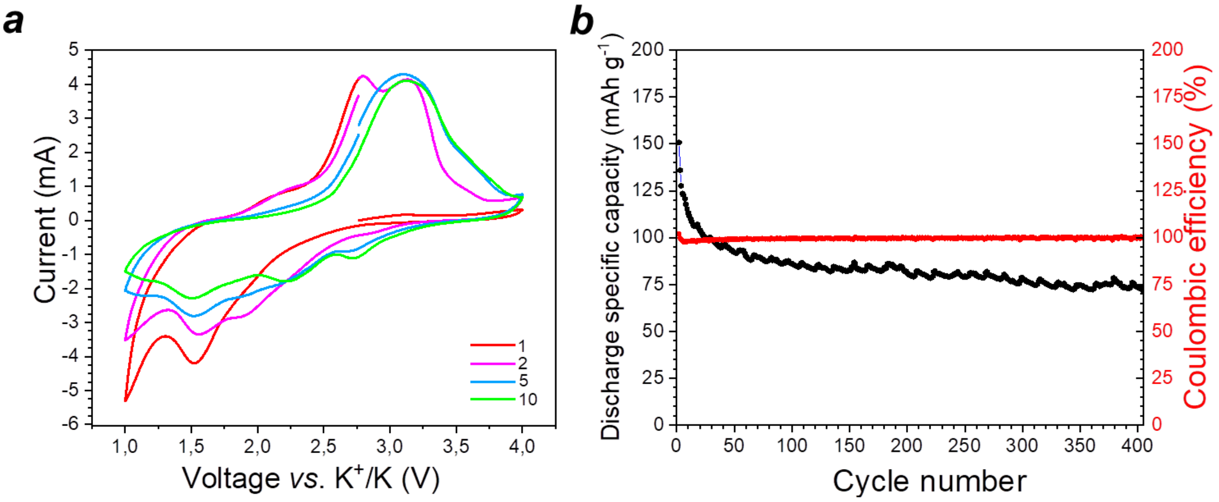

Figure S15. Cyclic voltammogram (a) and cycling performance at current density of 100 mA g^{-1} (b) of K//**NBI3** cells.

Experimental

Materials

Dianhydride of 1,4,5,8-naphtalenetetracarboxylic acid (NDA), 2,3-diaminophenazine, LiTFSI, KPF_6 were purchased from Macklin. 2,3,7,8-tetraaminophenazine was synthesized according to known procedure [J.K. Stille, E.L. Mainen, *Macromolecules*, 1968, **1**, 36]. N-methylpyrrolidone, pyridine, diethyl carbonate, 1,3-dioxolane, 1,2-dimethoxyethane, diglyme were purchased from Acros Organics and used without purification.

Synthesis of NBIs

NBI1. NDA (1.17 mmol), 2,3,7,8-tetraaminophenazine tetrahydrochloride (1.17 mmol), pyridine (4.68 mmol) and N-methylpyrrolidone (10 mL) were placed in a three-neck round-bottom flask with a magnetic Teflon-coated stirring bar and condenser. The system was degassed and filled with argon. The reaction mixture was refluxed for 6 hours under stirring and then cooled down to room temperature; the precipitate was isolated by filtration. The crude product was purified in a Soxhlet apparatus with diethyl carbonate and then dried in vacuo at 120°C. **NBI1** material appeared as deep cherry red powder (570 mg, 86%).

NBI2 was obtained similarly to **NBI1**, starting from 1.0 mmol of NDA, 0.5 mmol of 2,3,7,8-tetraaminophenazine tetrahydrochloride and 1.0 mmol of 2,3-diaminophenazine in 10 mL of NMP; 2 mmol of pyridine was added. **NBI2** appeared as a dark red powder (457 mg, 85%).

NBI3 was synthesized *via* a similar procedure starting from 2.0 mmol of NDA and 4.0 mmol of 2,3-diaminophenazine in 10 mL of NMP, without the addition of pyridine. The reaction mixture was refluxed for 6 hours and then cooled down to room temperature. Then, 20 mL of distilled water was added to the reaction mixture for complete precipitation of the product. For purification, ethanol was used instead of diethyl carbonate. **NBI1** appeared as dark red powder (1.14 g, 93%).

Material characterization

A Bruker Avance instrument (400 MHz for ^1H and 101 MHz for ^{13}C) (Bruker, Billerica, MA, USA) using a 3.2 mm MAS probe was used to record ssNMR spectra at room temperature. The Perkin Elmer Spectrum 100 (ZnSe prism) (PerkinElmer, Waltham, MA, USA). MALDI mass spectra were recorded using Axima Confidence time-of-flight spectrometer (Shimadzu Biotech) in the reflectron high resolution mode with a nitrogen laser (λ = 337 nm). Trans-2-[3-(4-tert-butylphenyl)-2-methyl-2-propenylidene]malononitrile (DCTB) (99%, Fluka) was used as a matrix.

Electrode preparation

Grinding of all the samples was performed using a Fritsch Pulverisette 7 system (Fritsch, Idar-Oberstein, Germany) equipped with zirconia jars and 1 mm zirconia balls. Materials were grinded with water for 30 min at 1000 rpm (25 cycles). Water was removed by freeze-drying.

Redox-active material (100 mg) and SuperC65 conductive carbon (MTI Corporation, USA) (80 mg) were thoroughly mixed in a mortar. Poly(vinylidenedifluoride) (Arkema, France) (20 mg) was solubilized in 0.8 mL of N-methylpyrrolidone. The composite of active material and SuperC65 was added to the PVDF solution. The resulting mixture was stirred for 16 h. Obtained slurry was tape-casted on carbon-coated Al foil, dried, and calendered at room temperature. Mass loadings of the active materials were in the range of ~0.8 mg cm^{-2}.

Cell assembling and testing

Circular electrodes were cut out; CR2032 coin-type cells were assembled in the argon-filled MBraun glove box (MBraun, Germany). For lithium coin cells, lithium discs were used as counter electrodes. 1 M LiTFSI solution in a 2:1 (v/v) mixture of 1,3-dioxolane and dimethoxyethane was used as the electrolyte (40 μL per cell). A single layer of glass fiber filter (Whatman GF/A, USA) was used as a separator. For potassium cells, metallic potassium was used as the counter electrode, 2.2 M solution of KPF_6 in diglyme was used as the electrolyte. For the cells with liquid alloy anodes, K-Na alloy (66:34 m/m) deposited on porous Ni discs was used as the counter electrode. 1 M KPF_6 in dimethoxyethane was used as the electrolyte (100 μL per cell), and two layers of glass fiber filter (Whatman GF/A, USA) were used as the separator.

For pouch cell assembly, rectangular electrodes (44×49.5 mm) were cut out and used as cathodes. Lithium sheets, rolled on thin Cu foil, were used as anodes. Battery terminals were prepared from Ni strips. 1 M LiTFSI solution in a 2:1 (v/v) mixture of 1,3-dioxolane and dimethoxyethane was used as the electrolyte (300 μL per cell), and a single layer of polypropylene (Celgard 2325, 25 μm; Celgard, USA) was used as a separator. Cell assembling was carried out in the argon-filled glove box using the Henkelman MiniJumbo vacuum packaging machine (Netherlands).

Cyclic voltammograms were recorded with Elins P40 or Elins P20 potentiostats (Elins, Russia). The charge-discharge tests were carried out using a Neware BTS3000 station (Neware, China); galvanostatic cycling started from the discharging for all of the cells.

Quantum chemical calculations

Structures of oligomers were optimized using the PBE exchange-correlation functional [*Phys. Rev. Lett*., 1996, **77**, 3865] and the SBK [*J. Chem. Phys*., 1984, **81**, 6026] pseudopotential. All molecular structures were optimized using the PRIRODA software package [*Chem. Phys. Lett*., 1997, **281**, 151], followed by the calculation of vibration frequencies to confirm their stability. The B3LYP/6-31G** level and the Gaussian03 program were used to calculate the energies of the frontier molecular orbitals. The Chemcraft software was used to visualize the molecular structures and molecular orbitals. All calculations were carried out at the Joint Supercomputer Center (JSCC).

The calculation of the specific metalation energies ΔE (eV) of the oligomer P

$$n\ \mathrm{M(metal)} + \mathrm{P} = \mathrm{PM}_n + n\ \Delta E$$

was performed based on the data for the theoretical energy of the reaction with diatomic molecules M_2 (M=K or Li)

$$n\ 0.5\ \mathrm{M}_2 + \mathrm{P} = \mathrm{PM}_n + n\ Q_n$$

taking into account the semi-empirical correction

$$\Delta E = Q_n - \delta,$$

based on the experimental values of the thermal effect of atomization of metallic potassium or lithium and the binding energy in the diatomic molecule M_2 (δ = 0.66 eV for K_2, 1.08 eV for Li_2).

While formation of both cis- and trans- isomers is possible for **NBIs1-3**, we have focused on the trans-isomers for calculation purposes (Fig. S16). Although isomer geometry influences the value of HOMO-LUMO gap, E_g values calculated for trans- and cis-isomeric NBI structures were very close (for **NBI2**: trans-isomer (E_g=1.93 eV), cis-isomer E_g=1.94 eV).

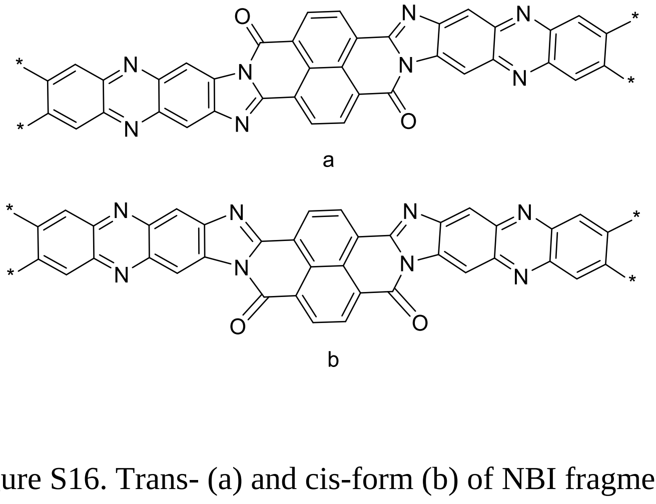

Figure S16. Trans- (a) and cis-form (b) of NBI fragment.

Oligomers were terminated with hydrogen atoms. Here we use “monomer number” as a number of NBI fragments. For example, for **NBI3**, the monomer number is 1, for **NBI2**, the monomer number is 2, etc (Fig. S17).

To investigate metal coordination during reductive metalation, stacks of two oligomers, located one above the other were used to ensure the coordination of M^+ by two similar redox-active groups of adjacent layers.

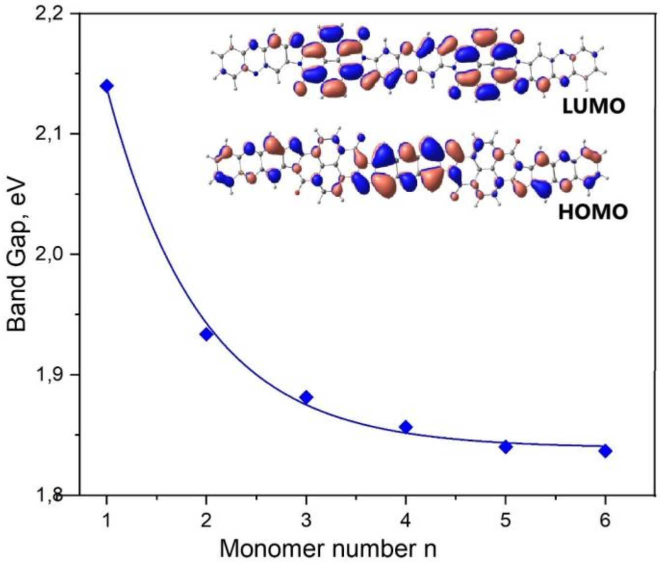

Figure S17. Band gap width as a function of the monomer number for NBIs calculated at the B3LYP/6-31G** level, defined as Eg = $E^{HOMO} - E^{LUMO}$, and molecular orbitals of **NBI2**.

HOMOs for the oligomers are mostly localized on the phenazine units, LUMOs are mostly localized on the NDI fragments. The band gap quickly decreases with an increase of the monomer unit number and becomes almost constant at n=6. This value is close to the experimental one for the polymer **NBI1** [*Macromolecules*, 2023, **56**, 5, 2081]. Preliminary calculations showed that the electron affinity (EA= - ε^{LUMO}) is 4.05, 4.18 and 4.20, 4.22 eV for oligomers with n = 1, 2, 3 and 4, respectively. Thus, the electron affinity, which is a key characteristic of oxidation-reduction processes, is saturated at $n \geqslant 2$ (**NBI2**).

For **NBI2** model, the initial distance between two layers is ~3.91Å. K^+ and Li^+ ions are coordinated between the layers. In this case, we observe K-O bonds longer than Li-O, as well as an increase in the distance between the layers during intercalation, as compared to the initial structure. With an increase in the degree of intercalation, the distance between the layers increases (Fig. S18).

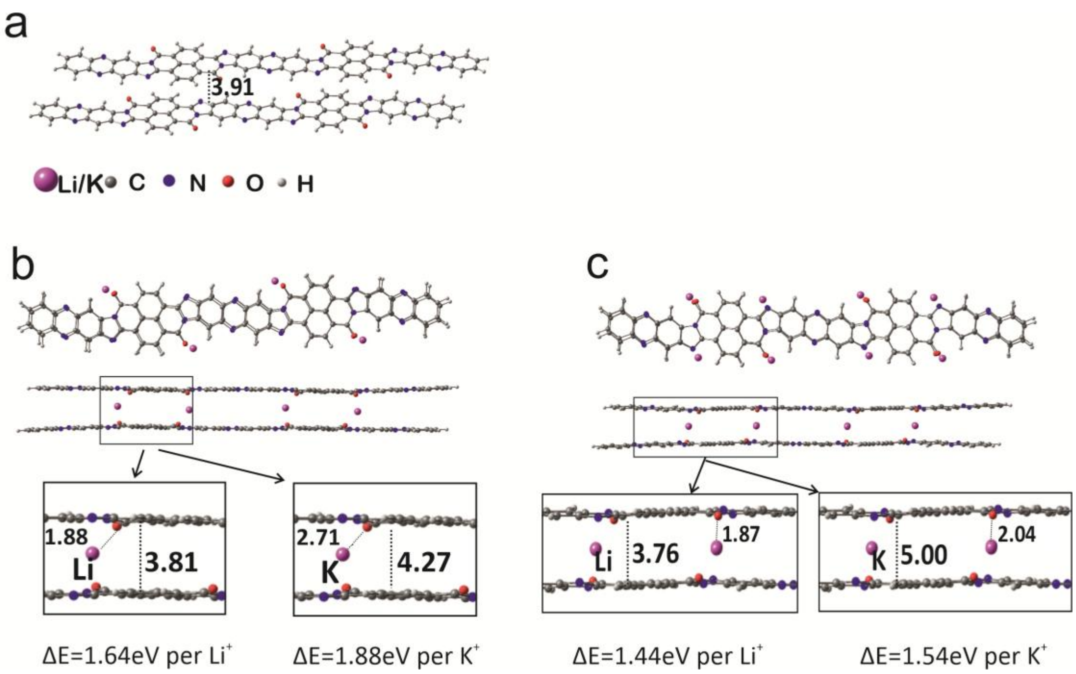

Figure S18. Two layers of **NBI2** (a), distance between the layers after the first step of metalation (b) and the second step of metalation (c), Å.

Two variants of two-layered **NBI2** with different relative shifts between the layers were investigated (Fig. S19). The first one is with C=O and phenazine centers of neighboring layers simultaneously participating in the coordination of one metal atom. The second one is with the C=O and N-C=N redox-active groups of neighboring layers participating in the coordination of one metal atom; phenazine sites remain free.

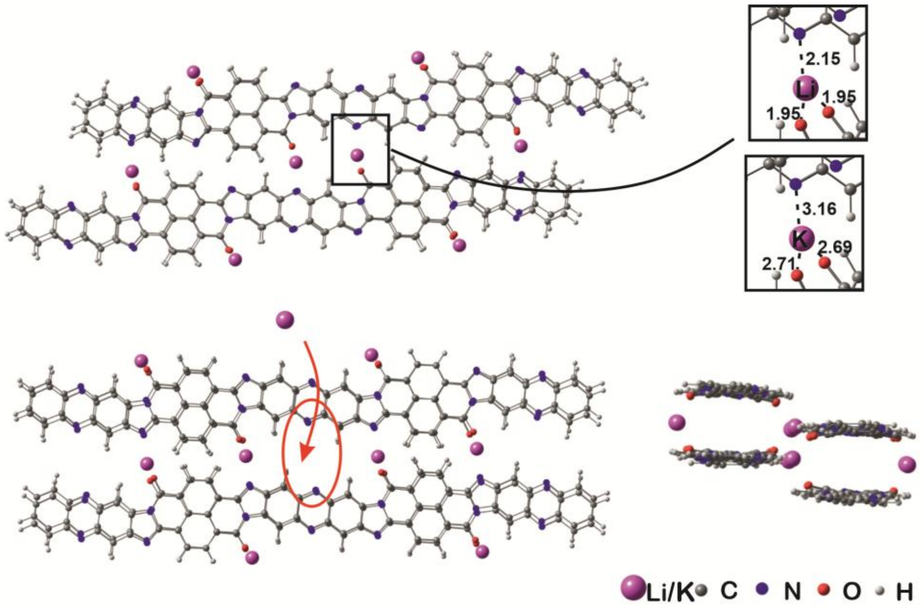

Figure S19. Metalated structures of two layers of **NBI2** with different relative shifts between the layers (top view, side view). Interatomic distances are given in the Å.

Formation of relatively long bonds during intercalation requires a significant disturbance of the rigid polymer structure. The experimentally observed lower capacities of the polymer cathode in potassium cells may be associated with this effect.

Table S1. Electrochemical performance of **NBI2** in potassium cells as compared to previously reported polyimide materials.

Material	Structure	Discharge specific capacity, mAh g^{-1}	Count of cycles	Capacity retention after cycling, %	Current density, A g^{-1}	Reference
PDPI/ CNTs-10	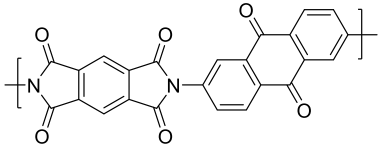	261	200	93	0.1	*Science Bulletin*, 2024, **69,** 3340
PI-CMP	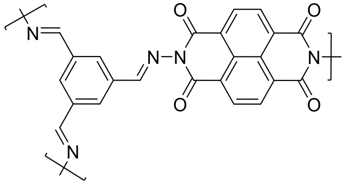	155	200	60	0.05	*J. Mater. Chem. A*, 2019, 7, 9997
PI-TAB	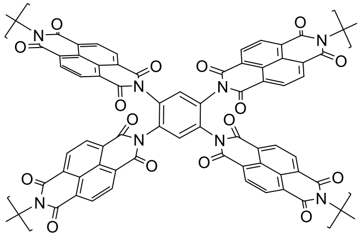	140	100	82	0.1	*ACS Appl. Mater. Interfaces*, 2022, **14**, 1, 826
PI@G	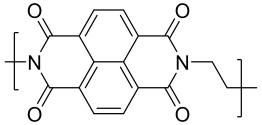	142	500	83	0.1	*ACS Appl. Mater. Interfaces*, 2019, **11**, 45, 42078

mPI	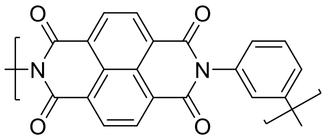	125	100	88	0.5	*ACS Appl. Energy Mater.*, 2021, **4**, 5, 4465
PIM@ KB	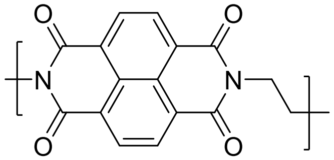	145	500	75	0.5	*Small*, 2020, **16**, 2002953
PIF	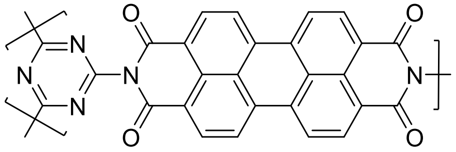	190	200	75	0.2	*Mater. Chem. Front.*, 2021, **5**, 7184
NBI2	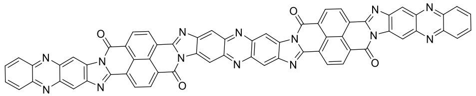	165	300	100	0.1	*this work*